Engineering MgFe2O4 nanoparticles to enhance magnetic, optical, and dielectric performance

Journal of Magnetism and Magnetic Materials 641 (2026) 173833

Contents lists available at ScienceDirect

Journal of Magnetism and Magnetic Materials

journal homepage: www.elsevier.com/locate/jmmm

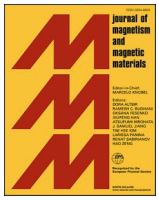

Engineering $MgFe_2O_4$ nanoparticles to enhance magnetic, optical, and dielectric performance☆

Muhammad Luqman Hashmi [a,b,*], Fabio Scaffidi Muta [c], Gianluca Deninno [c], C. Parmar [d], R. Verma [d], F. Mazaleyrat [e], Shashank N. Kane [d], Salil Modak [d], V.R. Reddy [f], Paola Maria Tiberto [b], Marco Coïsson [b]

[a] Politecnico di Torino, Torino, Italy
[b] Istituto Nazionale di Ricerca Metrologica, Torino, Italy
[c] Stellantis–Centro Ricerche Fiat, Torino, Italy
[d] Devi Ahilya University, Indore, India
[e] ENS, Paris, Saclay, France
[f] UGC-DAE Consortium for Scientific Research, Indore, India

ARTICLE INFO

Keywords:
$MgFe_2O_4$
Magnetic properties
M-H curves
Optical properties
Dielectric properties

ABSTRACT

This research investigated the effects of solution pH during synthesis and annealing on the structural, magnetic, optical, and dielectric properties of $MgFe_2O_4$ synthesised using the citric acid-assisted sol-gel auto-combustion method. Structural data showed that crystallinity, lattice parameters, and cation distribution were strongly influenced by both pH and annealing temperature. Optimal morphology and crystallinity were achieved at pH 7 and an annealing temperature of 550 °C for 3 h, under which cation ordering and defect reduction were effectively achieved. Magnetic characterisation revealed a significant improvement in saturation magnetisation (20.6 emu/g) under optimal conditions, attributed to increased super-exchange interactions. The optical bandgap was modulated by more than 11% (2.04 to 2.30 eV) by adjusting pH-mediated surface chemistry and subsequent defect states. The sample synthesised at pH 9 exhibited the highest values of ε', ε'', and σ_{ac}. These results conclusively demonstrate that accurate control of synthesis pH and annealing enables the design of multifunctional properties in $MgFe_2O_4$ nanoparticles, providing a solid foundation for their application in high-end magnetic, optical, and electronic devices.

1. Introduction

The synthesis of crystalline magnesium ferrite ($MgFe_2O_4$) nanoparticles is of great interest because of their potential applications in drug delivery, transformer cores, and high-frequency microwave devices. Careful control of synthesis is essential for optimising their performance for specific applications [1]. The crystal structure of magnesium ferrite, a partially inverted spinel, is represented by $(Mg_{1-\delta}Fe_{\delta})_A[Mg_{\delta}Fe_{2-\delta}]_BO_4$, where δ is the inversion parameter ranging between 0 and 1 [2]. The magnetic, electrical, and structural properties of $MgFe_2O_4$ are determined by how metal ions are distributed on A and B sites [3]. The preparation method and process conditions employed also affect these properties [2].

A common and low-cost method for synthesising oxide compounds is combustion synthesis [4], in which a self-sustaining exothermic reaction provides sufficient heat to sustain the process [5,6]. A drawback of using conventional fuels such as glycine or urea is inhomogeneous crystallite size, as demonstrated by earlier studies [7–9]. In this context, citric acid-based combustion reduces defect density by 40% compared with urea methods and promotes cation homogeneity in $CoFe_2O_4$ nanoparticles through metal ion chelation [7–9]. Despite these advancements, achieving phase purity in $MgFe_2O_4$ remains challenging, as samples obtained from sol-gel auto-combustion frequently contain more than 5 wt% residual α-Fe_2O_3 impurities [10].

Despite extensive recent studies on doped magnesium ferrite (e.g., Al-, Zn-, Ce-, Gd-, and Ni-doped $MgFe_2O_4$ systems) nanoparticles [11–17] synthesised via various combustion and hydrothermal methods, reports on green-synthesised pure magnesium ferrite remain

☆ This article is part of a Special issue entitled: 'SMM 27 advances' published in Journal of Magnetism and Magnetic Materials.

* Corresponding author at: Politecnico di Torino, Torino, Italy.
E-mail address: luqman.hashmi@polito.it (M.L. Hashmi).

https://doi.org/10.1016/j.jmmm.2026.173833
Received 2 October 2025; Received in revised form 31 December 2025; Accepted 10 January 2026
Available online 11 January 2026

limited, especially regarding pH-controlled synthesis conditions and post-synthesis thermal treatment, which can significantly affect its structural and functional properties. Green synthesis offers clear advantages in terms of environmental compatibility, reduced chemical load, and energy efficiency compared with conventional routes. Yet, its application to pure Mg-ferrite remains comparatively less explored. Therefore, the present work highlights the importance of controlled and environment-friendly synthesis conditions for pure Mg-ferrite nanoparticles, which can serve as a better baseline for further understanding of the stable structure and tunability of functional properties in Mg-ferrite systems.

The synthesis conditions for $MgFe_2O_4$, including pH, annealing temperature, and time, significantly affect its structural and functional properties [18]. The pH of the reaction medium is a critical synthesis parameter that strongly influences the surface chemistry of the precipitating nanoparticles, thereby affecting their structural and functional properties. According to Kosmulski [19–23], the surface charge of metal oxides in aqueous solution is highly pH-sensitive. When metal oxide surfaces adsorb H^+ or OH^- ions from the solution, they become charged. The pH at which the surface is electrically neutral is referred to as the point of zero charge, or PZC [19–23].

In $MgFe_2O_4$, the charge on the prevailing surface regulates the adsorption of Mg^{2+} and Fe^{3+} ions in solution, which governs their incorporation into the spinel lattice [24]. Below the PZC, a positively charged surface favours anion adsorption and may inhibit the uptake of Mg^{2+} and Fe^{3+}. A negatively charged surface favours cation adsorption above the PZC and therefore could inhibit anion adsorption [23], [25–30]. The stoichiometry and crystallinity of $MgFe_2O_4$ nanoparticles can be controlled by adjusting the pH. For example, non-stoichiometry or cation disorder can occur if a specific ion is selectively adsorbed at a particular pH. By carefully selecting the synthesis pH, the spinel structure can be tuned, thereby controlling the optical, dielectric, and magnetic properties [23], [25–30].

Annealing temperature is another key parameter for controlling the spinel ferrite structure. For instance, studies on the corresponding systems, i.e., Mg—W ferrites, indicate that increasing the annealing temperature enhances crystallite formation, reduces defect concentration, and improves phase purity, thereby directly affecting dielectric permittivity and magnetic permeability [31]. In $MgFe_2O_4$, superexchange interactions that govern magnetic behaviour are regulated by the geometric coordination of Mg^{2+} and Fe^{3+} ions at tetrahedral (A-site) and octahedral (B-site) positions. These interactions are influenced by thermal energy during annealing [32]. Annealing at elevated temperatures increases cation ordering, thus minimising lattice distortion and strain and optimising bandgap energies and charge-carrier mobility [33].

Optical properties, such as bandgap energy, are sensitive to defect states and crystallite size. Smaller crystallites, formed at lower annealing temperatures, produce surface defects and quantum confinement, resulting in bandgap narrowing. In contrast, higher temperatures produce larger crystallites, which reduce surface-to-volume ratios and tend to increase the bandgap, thereby enhancing light-absorption efficiency [34]. Moreover, dielectric properties such as permittivity and AC conductivity are governed by space-charge and interfacial polarisation phenomena, which are enhanced by improved crystallinity and reduced grain-boundary resistance at higher annealing temperatures [35].

Magnetic properties, i.e., saturation magnetisation (M_s) and coercivity (H_c), are directly related to the spinel structure inversion degree (δ) and oxygen positional parameter (u). Annealing facilitates diffusion of Fe^{3+} ions into octahedral sites, thereby enhancing A-O-B superexchange interactions and increasing M_s [36]. This interrelationship between annealing-induced improvements in functional properties and structural optimisation underscores the importance of thermal treatment in designing $MgFe_2O_4$ nanoparticles for specific applications.

Most of the literature on $MgFe_2O_4$ focuses on single-parameter optimisation, neglecting synergistic effects. Systematic studies examining the combined impact of synthesis pH and subsequent thermal treatment on the fundamental cation distribution in $MgFe_2O_4$ are limited. Therefore, this work addresses this gap by providing a comprehensive investigation into how pH-mediated surface charge and annealing-driven crystallite growth jointly influence the structural, magnetic, optical, and dielectric properties. Our goal is to go beyond single-parameter optimisation and develop a clear, predictive understanding of these complex relationships, offering a rational pathway for engineering $MgFe_2O_4$ nanoparticles with precisely tuned multifunctional properties.

2. Materials and methods

Magnesium Acetate [$(CH_3COO)_2Mg{\cdot}4H_2O$], Ferric Nitrate [$Fe(NO_3)_3{\cdot}9H_2O$], and Citric Acid ($C_6H_8O_7$) were used as precursors to synthesise MFO, with citric acid serving as both fuel and a chelating agent to facilitate the combustion reaction. The precursors were mixed with 10 mL of deionised water, maintaining a 1:1 M ratio of metal salt to citric acid. The pH (2 to 9) was controlled by adding suitable amounts of ammonia (NH_4OH) to the solution. This range was chosen to investigate the effects of various acidic and basic conditions during synthesis. These conditions influence the prevailing surface charge and regulate the adsorption of Mg^{2+} and Fe^{3+} ions in the solution, thereby governing their incorporation into the spinel lattice. The resulting solution was then dried in air at approximately 110 °C until a dry gel (fluffy powder) was obtained. To study the effect of annealing, the dry gel synthesised at pH 7 was annealed at 400 °C/2 h, 500 °C/2 h, 550 °C/3 h, and 600 °C/2 h. The rationale for these annealing conditions is that the desired crystalline phase forms prominently around 400–500 °C. Moreover, annealing at higher temperatures (e.g., above 600 °C or 700 °C) may lead to decomposition of the spinel phase into less desirable phases. Thus, the chosen annealing conditions were most suitable for investigating morphological and structural changes.

X-ray diffraction (XRD) was performed to analyse the crystal structure of the nanoparticles using a Bruker D8 Advance X-ray diffractometer with Cu Kα radiation (λ = 1.5406 Å). X-rays were detected with a fast-counting silicon-strip detector (Bruker LynxEye). The MAUD (Material Analysis Using Diffraction) program was used to perform the Rietveld refinement [37]. The experimental lattice parameter (a_{exp}), crystallite size ($D_{W\text{-}H}$), specific surface area (S), and defect density (ρ_D) were obtained from the XRD data. The XRD patterns were collected by scanning the 2θ range from 20° to 70°. The crystallite size ($D_{W\text{-}H}$) was estimated using the Williamson-Hall analysis [38], which accounts for XRD peak broadening due to grain size and associated microscopic strain effects, using the following equation:

$$\beta Cos\theta = \frac{K\lambda}{D} + 4\varepsilon Sin\theta \quad (1)$$

In this context, θ refers to the Bragg angle, β signifies the full width at half maximum (FWHM) of the diffraction peak, λ stands for the wavelength of the X-rays, K represents the Scherrer constant, valued at 0.94, and ε is the strain. Conventional techniques were used to optimise the lattice parameters. The cation distribution at tetrahedral and octahedral positions in the investigated material was established using Bertaut's method to analyse the XRD pattern [39].

A vibrating sample magnetometer (VSM) operating at room temperature, with a field range of −1 T (−10,000 Oe) < H < 1 T (10,000 Oe), was used to measure static magnetisation curves. The hysteresis loops were analysed to determine the values of saturation magnetisation (M_s), remanence (M_r), and coercivity (H_c) at room temperature [40].

UV–Vis diffuse reflectance spectra were recorded at room temperature using the PerkinElmer UV–Vis spectrometer (model Lambda 950) over the wavelength range 200–1500 nm. The energy bandgap was calculated using the Kubelka-Munk (K-M) Eq. [41].

$$F(R) = \frac{(1-R)^2}{2R} \quad (2)$$

Where R is the diffuse reflectance (%) and F(R) gives the absorption coefficient.

By plotting the K–M equation as a function of energy (in eV), the energy bandgap can be obtained from the TAUC plot by plotting $(F(R)\,h\nu)^2$ versus $h\nu$ and extrapolating to zero on the energy axis (x-axis).

Dielectric properties such as dielectric constant (ε'), dielectric loss (ε''), loss tangent ($tan\ \delta$), and AC conductivity (σ_{ac}) of the samples (10 mm diameter pellets) were measured over the frequency range of 100 Hz–1 MHz using Agilent Technologies E 4980 A LCR-meter.

Frequency-dependent ε', ε'', $tan\ \delta$, and σ_{ac} were obtained by using the following expressions [42]:

$$\varepsilon' = \frac{Cp \times d}{\varepsilon o \times A} \quad (3)$$

$$\varepsilon'' = (tan\delta) \times \varepsilon' \quad (4)$$

$$\sigma_{ac} = 2 \times \pi \times f \times \varepsilon'' \quad (5)$$

Where Cp is the parallel Capacitance, d is the pellet thickness, A is the pellet cross-sectional area, ε_o is the permittivity of free space, and f is the frequency.

3. Results and discussion

3.1. Morphological analysis (SEM)

Scanning Electron Microscopy (SEM) images (Fig. 1) show that particle morphology depends on the pH maintained during synthesis and on the annealing conditions. Fig. 1 **(a, b, c, and d)** shows that the average particle size decreases from 11 nm at pH 2 to 39 and 34 nm at pH 7 and 9, respectively. The sample synthesised at pH 2 exhibits a highly agglomerated structure with fine, poorly crystalline features. As the pH increases to 5, an apparent transition in morphology occurs, with both spherical and larger irregular nanoparticles present. There is

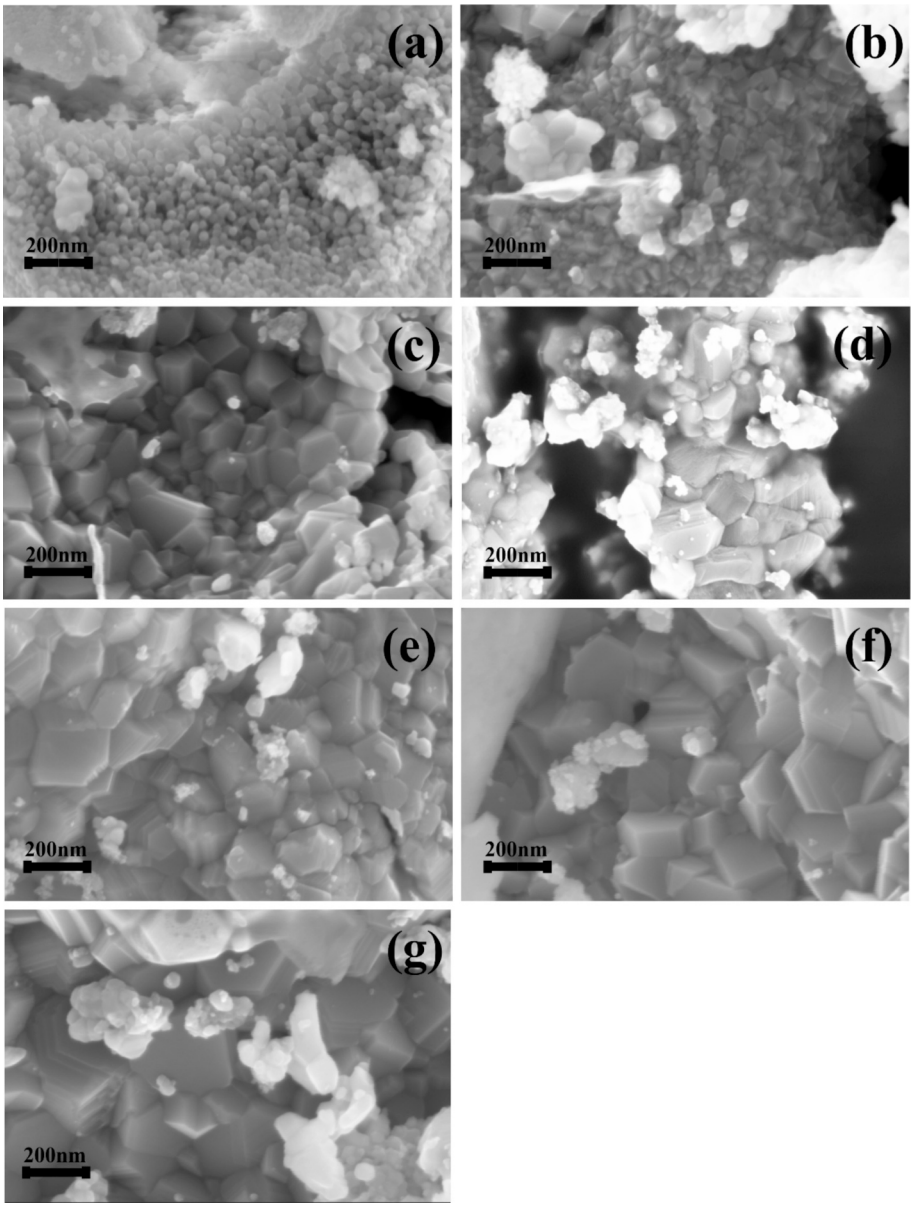

Fig. 1. SEM images of $MgFe_2O_4$ synthesised under conditions of (a) pH 2 and annealing at 550 °C for 3 h, (b) pH 5 and annealing at 550 °C for 3 h, (c) pH 7 and annealing at 550 °C for 3 h, (d) pH 9 and annealing at 550 °C for 3 h, (e) pH 7 and annealing at 400 °C for 2 h, (f) pH 7 and annealing at 500 °C for 2 h, and (g) pH 7 and annealing at 600 °C for 2 h.

noticeable agglomeration, but the individual particles appear slightly larger and more defined than in the pH 2 sample. The sample synthesised at pH 7 has the most uniform microstructure, with relatively uniform grain sizes. This microstructure indicates optimal surface-charge conditions for synthesis. At pH 9, increased agglomeration and a less uniform grain distribution are observed, likely due to excessive hydroxyl adsorption under the basic condition.

The effects of different annealing conditions (400 °C/2 h, 500 °C/2 h, 550 °C/3 h, and 600 °C/2 h) on morphology and particle size are shown in Fig. 1 **(c, e, f, and g)**. The sample annealed at 400 °C exhibits relatively poor crystalline features compared with samples annealed at higher temperatures. The particle size initially increases from 53 nm at 400 °C/2 h to 55 nm at 500 °C/2 h and then to 65 nm at 600 °C/2 h, consistent with enhanced grain growth at higher temperatures. However, the steep drop at 550 °C (39 nm) may be due to the more extended 3-h anneal, which promotes re-nucleation rather than growth.

The results of SEM analysis confirm that pH and annealing conditions are essential for controlling the microstructure of $MgFe_2O_4$ nanoparticles. Maintaining neutral pH during synthesis and then annealing at 550 °C for 3 h favours an optimal morphology for achieving multifunctional properties.

3.2. Structural evolution (XRD)

3.2.1. Structural evolution with pH

X-ray diffraction (XRD) patterns of $MgFe_2O_4$ samples synthesised at different pH values (2, 5, 7, and 9) show characteristic peaks for the cubic spinel structure of $MgFe_2O_4$ (Fig. 2). According to the standard PDF card in the ICDD database (Ref 01–071-1232), intense diffraction peaks are assigned to planes such as (220), (311), (400), (422), (511), and (440). A slight peak marked with an asterisk (*) is prominent at pH 7 and 9 and indicates the presence of α-Fe_2O_3 as an impurity phase.

The (311) peak is one of the most intense reflections in spinel ferrites and is highly sensitive to lattice parameter, strain, and cation distribution. The position of this peak varies slightly with pH. At pH 5, the peak shifts toward lower 2θ values compared with pH 2. It then approaches higher 2θ values as pH increases from 7 to 9 (Fig. 2). O'Neill et al. reported the experimental lattice parameter (a_{exp}) of stoichiometric $MgFe_2O_4$ to be 8.38–8.40 Å in 1992 [43]. Our investigations, however, observed a wider range of a_{exp} (8.28–8.34 Å) with a maximum at pH 5 (Table 1). a_{exp} decreased progressively as pH increased from acidic to basic, due to variations in cation distribution and strain effects. Thus, a peak shift toward lower or higher 2θ is attributed to lattice expansion or contraction caused by an increase (tensile strain) or decrease (compressive strain) in a_{exp}, respectively. However, these variations are just above the error bar; therefore, they represent a minimal, barely detectable (through XRD) lattice expansion or compression.

In parallel, the crystallite size (estimated using the Williamson-Hall analysis) increased with pH, reaching a maximum of 39 nm at pH 7 and then decreased slightly to 34 nm at pH 9. Dislocation density (ρ_D) decreased with increasing crystallite size, while surface area showed the anticipated inverse relationship with size (Table 1).

The distribution of cations between tetrahedral (A-site) and octahedral (B-site) positions was carefully examined using the inversion parameter (δ) and the oxygen positional parameter (u), as shown in Table 2. As pH increased from 2 to 7, Mg^{2+} ions predominantly occupied the A-sites. In contrast, Fe^{3+} ions were more strongly distributed on B-sites, resulting in a decrease in the inversion parameter (from 0.49 to 0.28). However, Mg^{2+} ions exhibited a notable preference for B-sites as pH increased to 9, while more Fe^{3+} ions shifted to A-sites, increasing the

Table 1
Experimental lattice parameter (a_{exp}), average crystallite size ($D_{w\text{-}h}$), specific surface area (S), and defect/dislocation density (ρ_D) of $MgFe_2O_4$ synthesised under different pH conditions and annealed at 550 °C/3 h.

pH	a_{exp} (nm) ±0.003	$D_{W\text{-}H}$ (nm) ±12	S (m^2/g) ±30	ρ_D (x10^{15}) (lines/m^2) ±2
2	0.831	11	122	9
5	0.834	23	57	2
7	0.832	39	33	0.7
9	0.828	34	38	0.9

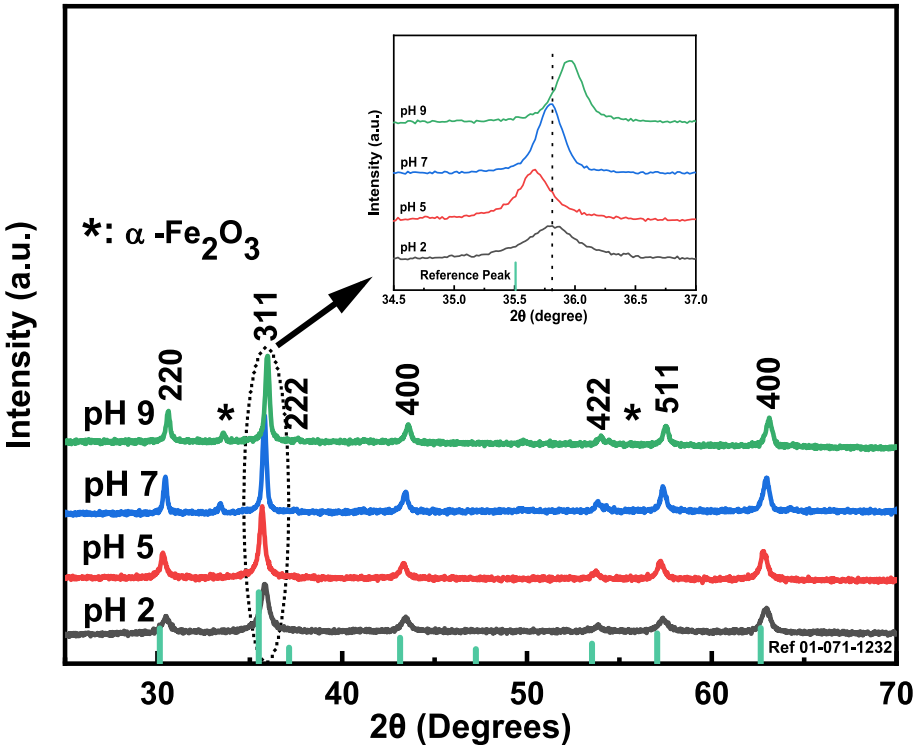

Fig. 2. XRD patterns of $MgFe_2O_4$ synthesised under different pH conditions and annealed at 550 °C/3 h.

Table 2
Cation distribution, oxygen positional parameter (u), and inversion parameter (δ) of $MgFe_2O_4$ synthesised under different pH conditions and annealed at 550 °C/3 h.

pH	Cation Distribution *A site B site*		u (±0.0002)	δ (±0.06)
2	$(Mg^{2+}_{0.51}Fe^{3+}_{0.49})$	$[Mg^{2+}_{0.49}Fe^{3+}_{1.72}]$	0.3827	0.49
5	$(Mg^{2+}_{0.72}Fe^{3+}_{0.28})$	$[Mg^{2+}_{0.28}Fe^{3+}_{1.72}]$	0.3834	0.28
7	$(Mg^{2+}_{0.72}Fe^{3+}_{0.28})$	$[Mg^{2+}_{0.28}Fe^{3+}_{1.72}]$	0.3838	0.28
9	$(Mg^{2+}_{0.49}Fe^{3+}_{0.51})$	$[Mg^{2+}_{0.51}Fe^{3+}_{1.49}]$	0.3832	0.51

inversion parameter (δ = 0.51). From Table 2, it is seen that u is somewhat larger than the ideal value (0.375) [44] but shows a slight decreasing trend with increasing δ, and vice versa. This can be ascribed to the shift of Mg^{2+} to the B position and of Fe^{3+} to the A position as δ increases. Owing to variations in ionic radii (Mg^{2+}: 0.72 Å, Fe^{3+}: 0.645 Å in tetrahedral coordination), the bond lengths of cation-oxygen are altered. For structural stability, oxygen atoms are drawn inward by A-site contraction due to the smaller Fe^{3+} and drawn outward by B-site expansion due to the larger Mg^{2+} [45,46]. The larger the inversion, the larger these opposing forces create a net oxygen sublattice shift, which manifests as a lower value of u [45]. This dynamic behaviour highlights the influence of pH on the positioning of cations within the structure.

It is worth noting that annealing at 550 °C for 3 h was used to probe the effect of pH, rather than testing the as-prepared samples. Indeed, this temperature provided the most suitable balance between crystallisation and property enhancement, as will be discussed in the following section. A recent study on sol-gel synthesised Yttrium-doped $MgFe_2O_4$ demonstrated that drying the gel at around 130 °C, followed by annealing at 800 °C, results in a nearly monophasic spinel phase with crystallite sizes of around 40 nm and much improved magnetic and structural characteristics. These findings indicate that annealing is not merely a routine thermal process but rather a critical step toward achieving phase purity, magnetic saturation, and reduced coercivity [47], and we therefore opted for it.

These findings show that the solution's pH is not merely a background condition but an essential tool for shaping the spinel structure, systematically transitioning from a highly inverted state ($\delta = 0.5$) at the acidic or basic extremes to a structure resembling normal spinel under neutral conditions. These structural results collectively demonstrate that pH 7 optimises cation ordering, crystallite size (39 nm), and reduces both defect density (0.7×10^{15} lines/m^2) and the inversion parameter (δ = 0.28), thereby justifying its choice for synthesising $MgFe_2O_4$.

3.2.2. *Structural evolution with annealing*

$MgFe_2O_4$ spinel ferrites prepared at pH 7 were systematically examined as a function of annealing temperature and time. The structural characteristics of $MgFe_2O_4$ as a function of temperature and time are shown in Fig. 3. According to the standard PDF card in the ICDD database (Ref 01–071-1232), X-ray diffraction (XRD) patterns confirmed a cubic spinel structure in all samples annealed at 400 °C, 500 °C, 550 °C, and 600 °C, as evidenced by intense diffraction peaks corresponding to the (220), (311), (222), (400), (422), (511), and (440) planes. No secondary phases were detected for shorter annealing times, indicating high phase purity. However, a slight peak marked with an asterisk (*) is prominent at 550 °C/3 h, indicating the presence of α-Fe_2O_3 as an impurity phase.

a_{exp} changed slightly with annealing temperature, ranging from 0.829 to 0.832 nm (Table 3). The largest a_{exp} was observed for the samples annealed at 400 °C and 550 °C (0.832 nm), and the smallest (0.829 nm) for the sample annealed at 600 °C. This change is insignificant given the error bars; however, the observed small changes in a_{exp}

Table 3
Experimental lattice parameter (a_{exp}), average crystallite size ($D_{w\text{-}h}$), specific surface area (S), and defect/dislocation density (ρ_D) of $MgFe_2O_4$ synthesised at pH 7 and different annealing conditions.

Ann. Temp./ Time	a_{exp} (nm) ±0.003	$D_{W\text{-}H}$ (nm) ±13	S (m^2/g) ±30	ρ_D (x10^{15}) (lines/m^2) ±2
400 °C/2 h	0.832	53	25	0.58
500°C/2 h	0.831	55	23	0.62
550 °C/3 h	0.832	39	33	0.65
600 °C/2 h	0.829	65	20	0.48

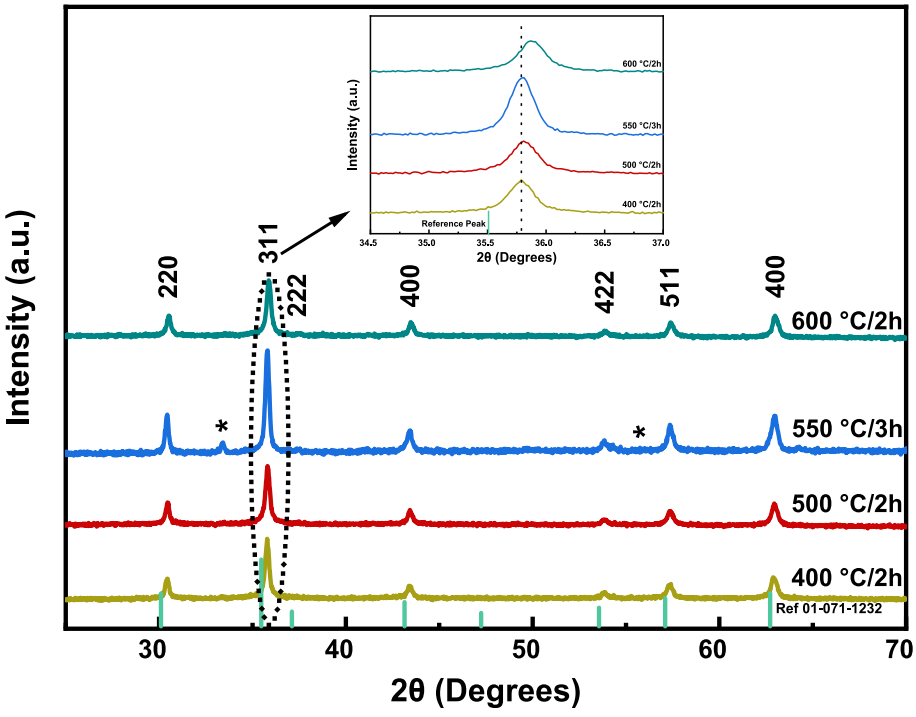

Fig. 3. XRD patterns of $MgFe_2O_4$ synthesised at pH 7 and different annealing conditions.

can be attributed to strain in the studied samples, ranging from 1.7 × 10^{-3} to 2.1 × 10^{-3}.

The crystallite size exhibited nonlinear behaviour with annealing (Table 3). It initially increased from 53 nm at 400 °C to 55 nm at 500 °C. There was a steep drop at 550 °C (39 nm), which may be because the more extended 3-h anneal promoted re-nucleation rather than growth, as observed, e.g., by Okoroh et al. [48], who reported that high-temperature annealed zinc ferrite nanoparticles exhibited particle size reduction as a result of surface melting effects that favour re-nucleation and structural reorganisation processes that suppress further crystallite growth. However, an increase to 65 nm at 600 °C for 2 h was observed, consistent with enhanced grain growth at elevated temperatures. Specific surface area (*S*) showed an inverse correlation with crystallite size (Table 3). This is consistent with what would be expected, since smaller crystallites create larger surface areas. Dislocation density (ρ_D) was maximum at 550 °C (0.65 × 10^{15} lines/m^2), supporting defect accumulation due to reduced grain size with increasing annealing time. Conversely, the minimum dislocation density at 600 °C (0.48 × 10^{15} lines/m^2) was suggestive of improved crystallinity due to thermal defect annihilation (Table 3).

The distribution of cations in spinel ferrites is strongly influenced by annealing, as shown in Table 4. Spinel was highly inverted, decreasing slightly from 400 °C/2 h to 600 °C/2 h (δ decreased from 0.77 to 0.70), with more Fe^{3+} migrating to A-sites and Mg^{2+} to B-sites. A notable effect of annealing time was that at 550 °C/3 h, the structure reverted to a normal spinel ($\delta = 0.28$), with most Mg^{2+} ions on A-sites and Fe^{3+} ions migrating to B-sites. The oxygen positional parameter (*u*) was again inversely correlated with δ, ranging from 0.3811 to 0.3838 (Table 4).

This analysis reveals a critical insight that annealing time appears to be a more dominant factor than annealing temperature in governing the final cation distribution. The dramatic drop in the inversion parameter to $\delta = 0.28$ for the 550 °C/3 h sample, compared with the highly inverted state ($\delta \geq 0.70$) of all samples annealed for 2 h, indicates a kinetically driven reordering process. This finding is crucial for synthesis design, as it shows that a specific thermal budget (time at temperature) is required to overcome the kinetic barrier and achieve the more stable, less inverted spinel structure.

3.3. Magnetic properties

3.3.1. Magnetic properties with pH

Magnetic properties of $MgFe_2O_4$ as a function of pH are presented in Fig. 4 and Table 5. Saturation magnetisation (M_s) increases from a very low value at pH 2 (13.5 emu/g) to a peak at pH 7 (20.6 emu/g) and then decreases slightly at pH 9 (19.4 emu/g). The highest saturation magnetisation is observed when crystallinity is best, and the cation distribution enables strong superexchange coupling between the A and B sites (see Fig. 2 and Table 2). Remanence (M_r) also tracks saturation magnetisation. Low M_s at pH 2 can be attributed to several factors, including a very high defect density and a large surface area. A high surface area, due to the small size of the crystallites, implies extensive surface spin disorder, which drastically lowers the magnetisation. High inversion (more Fe^{3+} ions in the A-site) is detrimental to the magnetic moment because it interferes with the perfect antiparallel arrangement of A- and B-site spins. The rise in M_s up to pH 7 is due to reduced inversion and increased crystallite size, which reduces surface spin disorder. More Mg^{2+} occupancy at A sites and Fe^{3+} occupancy at B sites strengthen superexchange interactions between A and B sites, forming a larger net magnetic moment. The slight reduction in M_s at pH 9 can be ascribed to a trivial decrease in crystallite size (increasing surface spin disorder) and to an increased inversion degree. With a greater proportion of Fe^{3+} ions filling positions in the A-sites, there is less net magnetic moment.

The coercivity (H_c) of $MgFe_2O_4$ increases from 34 Oe at pH 2 to a maximum of 96 Oe at pH 7, then plateaus at 97 Oe at pH 9. This trend reflects the interplay of several factors. At lower pH, a smaller crystallite size and a very high defect density lead to single-domain behaviour but disrupted magnetic order. In contrast, at pH 7, optimal cation ordering and a larger crystallite size strengthen the A-B superexchange interaction. The observed higher coercivity can be attributed to increased anisotropy, which enhances domain-wall pinning.

$MgFe_2O_4$ nanoparticles usually have lower M_s values than bulk $MgFe_2O_4$ due to surface and size effects that disrupt magnetic ordering [49]. Bulk Mg ferrite has been reported to have M_s values of around 27 emu/g by Smit and Wijn [50] and Kulkarni and Joshi [51]. Bulk magnetite (Fe_3O_4) has a higher M_s value of around 90 emu/g. Magnetite nanoparticles have smaller M_s values, typically in the range of 30–50 emu/g [52].

The peak saturation magnetisation ($M_s = 20.6$ emu/g) at pH 7 results directly from the optimised cation distribution ($\delta = 0.28$) achieved at that pH. Therefore, pH can serve as a precise tool for controlling Fe^{3+} site occupancy, thereby maximising A-B superexchange interactions and improving magnetic properties without requiring elemental doping.

3.3.2. Magnetic properties with annealing

Magnetic characteristics of $MgFe_2O_4$ under varying annealing conditions are presented in Fig. 5 and Table 6.

M_s varied non-monotonically with the annealing temperature. It was 20.6 emu/g at 400 °C/2 h. It reduced to 17.5 emu/g at 500 °C/2 h and slightly improved to 18 emu/g at 600 °C/2 h. At 550 °C/3 h, the hysteresis loop and M_s are nearly identical to those at 400 °C/2 h, despite structural differences (Fig. 5). The high M_s at 400 °C/2 h, despite the highest inversion degree, can be linked to a large crystallite size (lower surface spin disorder). The anomalous retention of M_s at 550 °C/3 h coincides with cations inverting back toward a normal spinel (the majority of Mg^{2+} ions on A-sites and Fe^{3+} migrating to B-sites), thereby enhancing A-B superexchange interactions. At 500 °C and 600 °C, the inverse spinel structure is nearly the same as at 400 °C/2 h. Still, Ms. is slightly reduced, which may indicate multidomain formation due to the comparatively larger grain size, limiting complete domain alignment under the applied field. Thus, obtaining the optimum grain size is essential for tuning M_s to higher levels. M_r also exhibited the same phenomenon, with a maximum of 6.2 emu/g observed at 550 °C/3 h, indicating mature magnetic ordering.

H_c reaches higher values at a lower annealing time (2 h), possibly because the much larger grain size has greater anisotropy and reduced surface demagnetising effects. The sample annealed at 500 °C/2 h has H_c value of 110 Oe, which is almost 15% higher than other conditions.

Thus, varying annealing conditions strongly influence magnetic properties through structural changes. The cation distribution is the governing factor in magnetic behaviour. Greater occupancy of B-sites by Fe^{3+} ions, as observed at 550 °C/3 h, enhances magnetic interactions and increases M_s and M_r. Lower crystallite size promotes higher surface disorder; however, an optimised cation arrangement may counteract this by increasing magnetisation.

Table 4
Cation distribution, oxygen positional parameter (u), and inversion parameter (δ) of $MgFe_2O_4$ synthesised at pH 7 and different annealing conditions.

Ann. Temp./Time	Cation Distribution A site	B site	*u* (±0.0002)	*δ* (±0.06)
400 °C/2 h	$(Mg^{2+}_{0.23}Fe^{3+}_{0.77})$	$[Mg^{2+}_{0.77}Fe^{3+}_{1.23}]$	0.3811	0.77
500°C/2 h	$(Mg^{2+}_{0.26}Fe^{3+}_{0.74})$	$[Mg^{2+}_{0.74}Fe^{3+}_{1.26}]$	0.3814	0.74
550 °C/3 h	$(Mg^{2+}_{0.72}Fe^{3+}_{0.28})$	$[Mg^{2+}_{0.28}Fe^{3+}_{1.72}]$	0.3838	0.28
600 °C/2 h	$(Mg^{2+}_{0.30}Fe^{3+}_{0.70})$	$[Mg^{2+}_{0.70}Fe^{3+}_{1.30}]$	0.3818	0.70

3.4. Optical properties

This work presents a novel, non-doping approach to tailoring the optical absorption profile of magnesium ferrite. The UV–Vis absorption spectra of $MgFe_2O_4$ (Fig. 6), synthesised at different pH values, exhibit distinct absorption behaviours, reflecting changes in electronic

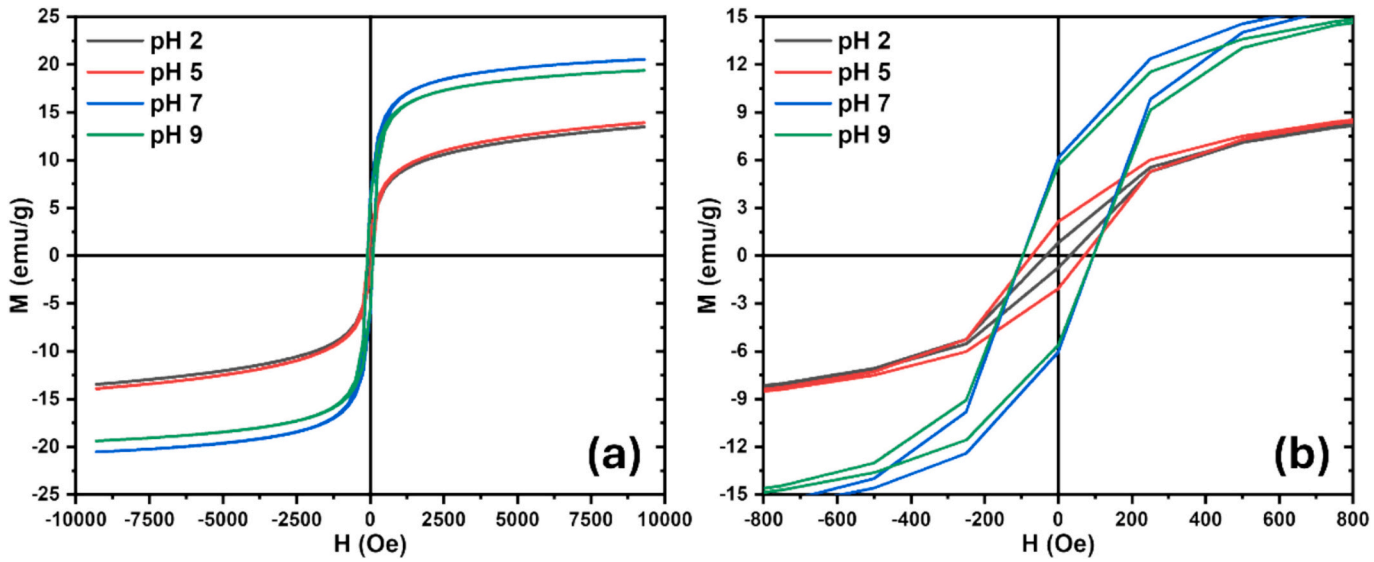

Fig. 4. (a) Hysteresis loops of $MgFe_2O_4$ synthesised under different pH conditions and annealed at 550 °C/3 h, (b) magnification of hysteresis loops at low magnetic fields demonstrates variations in coercivity.

Table 5
Saturation magnetisation (M_s), remanence (M_r), and coercivity (H_c) of $MgFe_2O_4$ synthesised under different pH conditions and annealed at 550 °C/3 h.

pH	Saturation Magnetisation (M_s) (emu/g)	Remanence (M_r) (emu/g)	Coercivity (H_c) (Oe)
2	13.5	0.8	34
5	13.9	2.1	72
7	20.6	6.2	96
9	19.4	5.7	97

transitions and structural properties. The absorption bands in the ultraviolet region appear below 400 nm, whereas the visible spectrum up to 600 nm is less absorbed [53,54].

The band gap energy (E_g) of $MgFe_2O_4$ was calculated from UV–Vis spectra using Tauc plots, which are plots of $(\alpha h\nu)^2$ versus photon energy ($h\nu$). E_g values ranged from 2.04 eV (pH 2) to 2.30 eV (pH 5), 2.10 eV (pH 7), and 2.25 eV (pH 9). This trend reflects a subtle balance among crystallinity, cation distribution (inversion parameter δ), crystallite size, and defect density. A partial inverse spinel structure of $MgFe_2O_4$ results in a narrower electronic band gap because Fe^{3+} occupies both octahedral and tetrahedral positions [55]. At pH 2, higher inversion ($\delta = 0.49$) leads to a greater number of Fe^{3+} ions in tetrahedral sites, reducing the band gap. Moreover, the observed narrowing (2.04 eV) suggests defect-mediated mid-gap states owing to a very high defect density (9×10^{15} lines/m^2) [56], leading to tailing of the absorption edge, commonly modelled using Urbach energy concepts [57]. These defect states effectively narrow the band gap by facilitating sub-bandgap transitions. The highest pH values during synthesis (5–9) yielded higher Eg values, attributed to larger crystallite sizes (improved crystallinity) [34] and a reduced density of defect-related states. At pH 5, lower inversion ($\delta = 0.28$), indicating fewer Fe^{3+} ions in tetrahedral sites than at pH 2, matches better cation ordering and expands the E_g. At pH 7, δ is low at 0.28, which would otherwise be in accordance with a wider band gap. The counter effect of secondary phase α-Fe_2O_3 absorption and/or overlapping defect states leads to a net decrease in observed E_g.

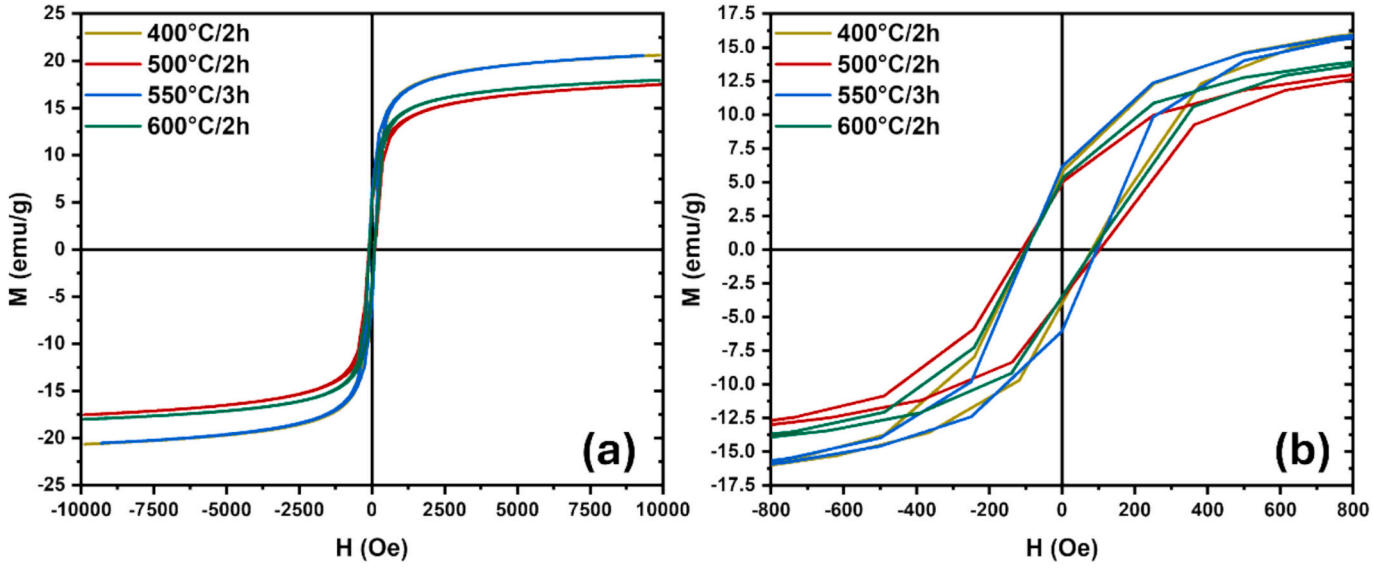

Fig. 5. (a) Hysteresis loops of $MgFe_2O_4$ synthesised at pH 7 and different annealing conditions, (b) magnification of hysteresis loops at low magnetic fields demonstrates variations in coercivity.

Table 6
Saturation magnetisation (M_s), remanence (M_r), and coercivity (H_c) of $MgFe_2O_4$ synthesised at pH 7 and different annealing conditions.

Temp./ Time	Saturation Magnetisation (Ms) (emu/g)	Remanence (Mr) (emu/g)	Coercivity (Hc) (Oe)
400 °C/2 h	20.6	5.6	100
500 °C/2 h	17.5	4.9	110
550 °C/3 h	20.6	6.2	96
600 °C/2 h	18.0	5.1	100

This work shows that the bandgap is influenced by two pH-dependent factors: (1) defect-mediated mid-gap states, which reduce the E_g at low pH, and (2) the cation distribution (δ), which increases the E_g as the structure trends toward a normal spin. The bandgap of $MgFe_2O_4$ can be precisely adjusted by more than 11% (from 2.04 eV to 2.30 eV) solely by pH control.

3.5. Dielectric properties

Variation of dielectric properties like dielectric constant (ε'), dielectric loss (ε''), loss tangent ($tan\ \delta$), and AC conductivity (σ_{ac}), with frequency for $MgFe_2O_4$ over a pH range of 2 to 9 are shown in Fig. 7. At low frequencies, ε', ε ", and *tan* δ have high values, which reduce progressively as frequency increases until one gets a plateau at high frequencies. Koops' theory anticipates that the composite system will have a high ε' at low frequencies due to polarisation processes that enable charge accumulation at the interface [58]. The composite system in this case refers to conducting grains and less-conducting or insulating grain boundaries in ferrites [59]. At higher frequencies, however, rapid ions (dipoles) cannot keep up with the rapidly changing electric field, and ε' is smaller. This is described by a heterogeneous conduction mechanism that results in space-charge polarisation [58,60,61].

ε'' is equivalent to the energy dissipation within the material. The highest ε' and ε'' are observed at pH 9, followed by pH 7 and pH 2, and the lowest is observed for the sample at pH 5, as shown in Figs. 7(a) and 7(b). The loss tangent ($tan\ \delta = \varepsilon''/\varepsilon'$) indicates the ratio of energy lost to energy stored in a material and shows a somewhat different trend with pH, as pH 5 has a different influence on *tan* δ than on ε' and ε''. At low frequencies, pH 5 has higher *tan* δ values than those for pH 7 and pH 2. The *tan* δ exhibits dispersion at low frequencies, as illustrated in Fig. 7 **(c)**. Under an AC electric field, the *tan* δ values decrease and exhibit frequency-independent behaviour at high frequencies. Larger loss values of ε'' and *tan* δ at lower frequencies suggest the weak conduction at grain boundaries and larger energy dissipation due to hopping between Fe^{2+} and Fe^{3+} ions [62–64]. But the grains are highly conductive at high frequencies, and electron interactions between Fe^{2+} and Fe^{3+} cause minor energy dissipation [60,65]. In general, the magnitude of *tan* δ is a function of increasing pH.

AC conductivity (σ_{ac}), shown in Fig. 7 **(d)**, increases with increasing frequency for all samples. This is expected because, at high frequencies,

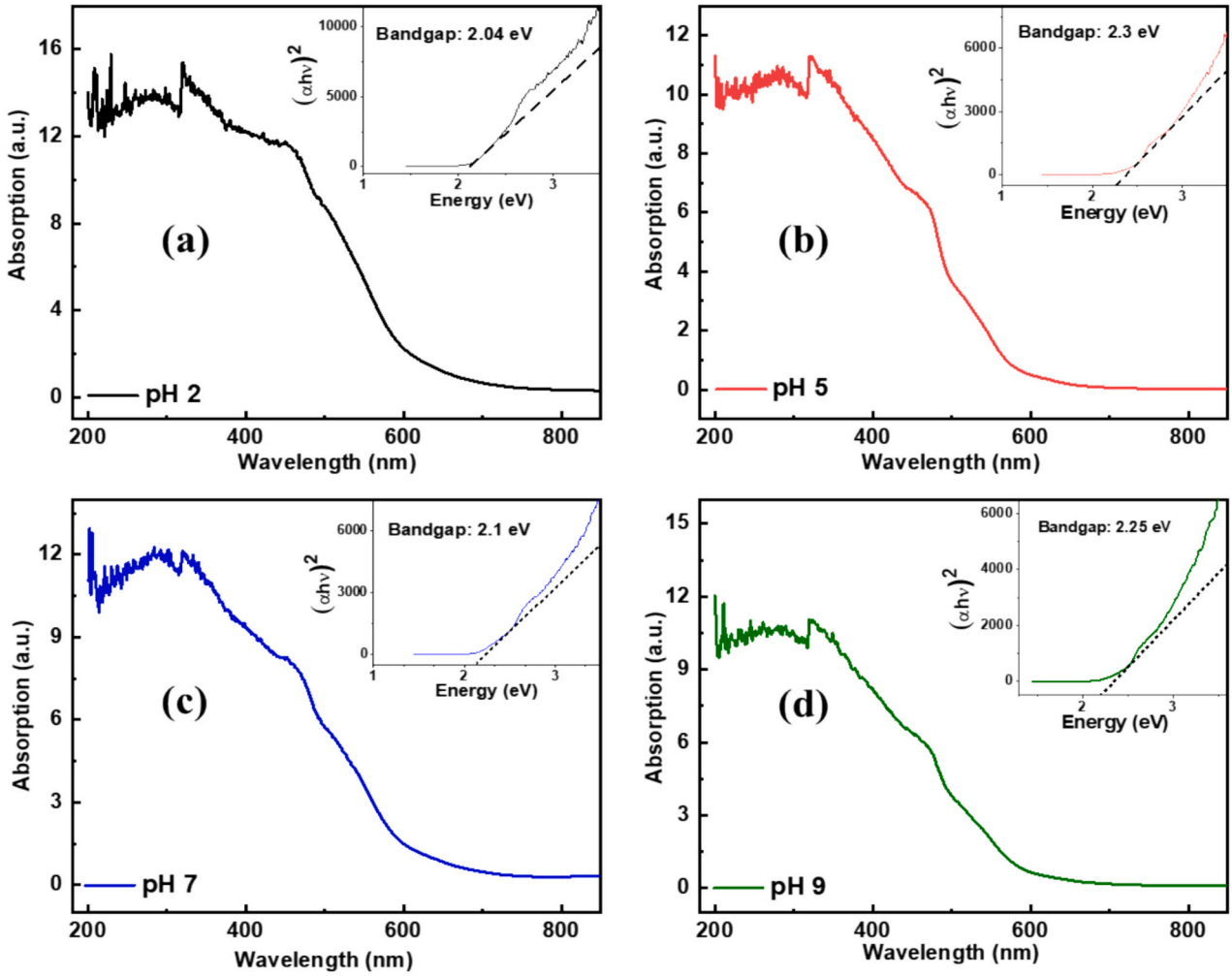

Fig. 6. UV/visible absorbance spectra of $MgFe_2O_4$ annealed at 550 °C/3 h and varying pH: (a) pH 2, (b) pH 5, (c) pH 7, and (d) pH 9.

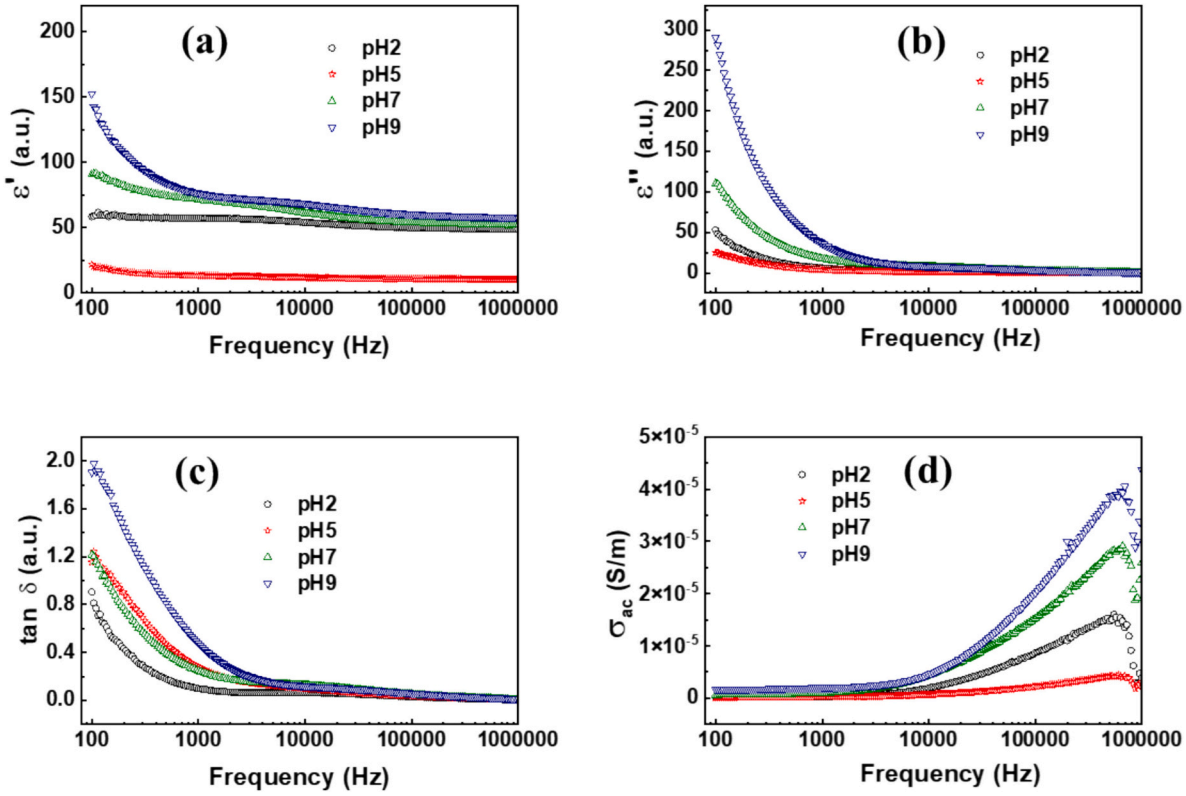

Fig. 7. Dielectric properties of $MgFe_2O_4$ at 550 °C/3 h in a pH range of 2 to 9: (a) dielectric constant (ε'), (b) dielectric loss (ε''), (c) loss tangent ($tan\ \delta$), and (d) AC conductivity (σ_{ac}).

charge carriers can easily hop between localised states, increasing conductivity; in accordance with Jonscher's law [66]. The sample prepared at pH 9 has the highest $\sigma_{ac,}$ followed by pH 7 and pH 2, while the sample at pH 5 has the least.

The structural change induced by modifying the pH level during synthesis directly affects the dielectric properties of $MgFe_2O_4$ nanoparticles. The cation distribution has a profound impact. The distribution of Mg^{2+} and Fe^{3+} ions at A and B sites controls electron hopping among Fe^{2+} and Fe^{3+} ions and thus the dielectric loss and conductivity [62–64]. In addition, ε' is affected by the increase in grain size (crystallite size). Larger grains have fewer grain boundaries, reducing charge-carrier scattering and enhancing polarisation [64]. This could be why the pH 7 sample (larger grain size) is seen to have a higher ε' than the pH 2 sample (smaller grain size).

This analysis establishes a novel connection between the pH-engineered cation distribution and the material's dielectric response, which can be precisely controlled solely by pH. The characteristic frequency-dependent ferrite behaviour was observed, with the sample synthesised at pH 9 exhibiting the highest ε', ε'', and σ_{ac}, while pH 2 and pH 5 yielded lower values.

4. Conclusions

The interrelationships among synthesis conditions, structural properties, and functional characteristics determined in this investigation constitute an integrated platform for the rational design of spinel ferrite nanoparticles with specified performance. pH and annealing conditions, separately and collectively, affect the structural, magnetic, optical, and dielectric properties of $MgFe_2O_4$ nanoparticles synthesised by a citric acid-assisted sol-gel auto-combustion route. A neutral pH of 7 and 3 h of annealing at 550 °C are optimal conditions that yield the best balance among high crystallinity, good cation ordering, and low defect density. Under these conditions, an optimal morphological structure, a minimum inversion parameter (δ = 0.28), better cation ordering, a controlled crystallite size (~39 nm), and a reduced defect density (0.7×10^{15} lines/m^2) were achieved, resulting in stronger superexchange coupling and the highest saturation magnetisation of $MgFe_2O_4$ (20.6 emu/g). Structural investigation reveals that the inversion parameter and the oxygen positional parameter can be precisely modulated through variation in synthesis conditions, offering a way to tune the spinel structure and, therefore, the magnetic and dielectric response. Furthermore, our research proves that the optical bandgap and the dielectric properties can be systematically varied through rational modification of synthesis conditions, enhancing the technological applicability of $MgFe_2O_4$ nanoparticles. It was observed that the optical bandgap was not static but could be modulated by more than 11% (2.04 to 2.30 eV) solely by adjusting the pH-mediated surface chemistry and the resulting defect states. The characteristic frequency-dependent ferrite behaviour was observed, with the sample synthesised at pH 9 exhibiting the highest ε' and ε'' and σ_{ac}, while pH 2 and pH 5 yielded the minimum values. Therefore, synthesis pH serves as a critical tuning parameter for optimising the material's energy storage and transport capabilities according to the Maxwell-Wagner polarisation model.

CRediT authorship contribution statement

Muhammad Luqman Hashmi: Writing – original draft, Investigation, Formal analysis, Data curation, Conceptualization. **Fabio Scaffidi Muta:** Validation. **Gianluca Deninno:** Validation. **C. Parmar:** Data curation. **R. Verma:** Validation, Data curation. **F. Mazaleyrat:** Validation. **Shashank N. Kane:** Writing – review & editing, Validation, Formal analysis, Data curation. **Salil Modak:** Validation, Formal analysis, Data curation. **V.R. Reddy:** Validation. **Paola Maria Tiberto:** Writing – review & editing, Visualization, Validation. **Marco Coïsson:** Writing – review & editing, Supervision, Conceptualization.

Declaration of competing interest

The authors declare that they have no known competing financial interests or personal relationships that could have appeared to influence the work reported in this paper.

Acknowledgements

SNK and SM acknowledge gratefully the support received from the project ANRF/PAIR/2025/000018/PAIR.

Data availability

Data will be made available on request.

References

[1] R. Valenzuela, Novel applications of ferrites, Physics Research International 2012 (1) (2012) 591839.
[2] S.M. Antao, I. Hassan, J.B. Parise, Cation ordering in magnesioferrite, MgFe2O4, to 982°C using in situ synchrotron X-ray powder diffraction, Am. Mineral. 90 (1) (2005) 219–228.
[3] F. Farshidfar, M. Lapolla, A. Fattahi, K. Ghandi, On the structural and electrical properties of MgFe2O4, MgMn0. 2Fe1. 8O4, and Mn3O4, Heliyon 9 (11) (2023).
[4] A.S. Mukasyan, A.S. Rogachev, S.T. Aruna, Combustion synthesis in nanostructured reactive systems, Adv. Powder Technol. 26 (3) (2015) 954–976.
[5] S.T. Aruna, A.S. Mukasyan, Combustion synthesis and nanomaterials, Curr. Opinion Solid State Mater. Sci. 12 (3–4) (2008) 44–50.
[6] A. Sutka, G. Mezinskis, Sol-gel auto-combustion synthesis of spinel-type ferrite nanomaterials, Front. Mater. Sci. 6 (2012) 128–141.
[7] A.B. Salunkhe, V.M. Khot, M.R. Phadatare, N.D. Thorat, R.S. Joshi, H.M. Yadav, S. H. Pawar, Low temperature combustion synthesis and magnetostructural properties of co–Mn nanoferrites, J. Magn. Magn. Mater. 352 (2014) 91–98.
[8] M.H. Yousefi, S. Manouchehri, A. Arab, M. Mozaffari, G.R. Amiri, J. Amighian, Preparation of cobalt–zinc ferrite (Co0. 8Zn0. 2Fe2O4) nanopowder via combustion method and investigation of its magnetic properties, Mater. Res. Bull. 45 (12) (2010) 1792–1795.
[9] T. Dippong, E.A. Levei, O. Cadar, Recent advances in synthesis and applications of MFe2O4 (M= co, cu, Mn, Ni, Zn) nanoparticles, Nanomaterials 11 (6) (2021) 1560.
[10] N. Kumari, R. Jasrotia, S. Kour, N. Neha, Y. Singh, R. Kumar, Synthesis methods and magnetic properties of magnesium ferrites: A short review, in: AIP Conference Proceedings 2357, No. 1, AIP Publishing, 2022, May.
[11] C.B. Naidu, Effect of Microwave Heat Treatment on Hydrothermal Synthesis of Nano-MgFe2O4, 2020.
[12] N. Venkatesh, D.R. Kumar, S. Goud, S.I. Ahmad, P. Veerasomaiah, D. Ravinder, Structural, photocatalytic, electromagnetic properties of rare-earth metal Gd-doped Mg nanoferrites synthesized by citrate gel auto-combustion method, Chem. Pap. 77 (5) (2023) 2749–2767.
[13] R. Srimathi, N.S. Rao, A. Merlin, R. Kiruthika, A. Selvaraj, O.H. Abdelkader, L. Rajadurai, Investigation of structural, magnetic, optical and dielectric characteristics of Al-doped MgFe2O4 nanoparticles, Solid State Sci. 159 (2025) 107761.
[14] T.S. Kumar, G. Sriramulu, P. Raju, T. Ramesh, K. Praveena, S. Katlakunta, Structural, optical, magnetic and dielectric properties of Ce-doped MgFe2O4 prepared by microwave hydrothermal method, ECS J. Solid State Sci. Technol. 12 (9) (2023) 093014.
[15] A. Manohar, C. Krishnamoorthi, K.C.B. Naidu, B.P. Narasaiah, Dielectric, magnetic hyperthermia and photocatalytic properties of $Mg_{0.7}Zn_{0.3}Fe_2O_4$ nanocrystals, IEEE Trans. Magn. 56 (12) (2020) 1–7.
[16] R. Revathi, M. Sukumar, A. Kumar, M. Gupta, P.A. Udhaya, S.S. Sehgal, M. Ubaidullah, Facile synthesis of Ni2+ doped MgFe2O4 spinel nanoparticles: structural, optical, magnetic, and dielectric behavior, Journal of Inorganic and Organometallic Polymers and Materials 34 (1) (2024) 374–386.
[17] L. Rajadurai, N.S. Rao, M. Sundararajan, M. Gupta, K. Sharma, S. Yuvaraj, M. Sukumar, Facile synthesis, characterization, and dielectric properties of Zn2+ substituted MgFe2O4 spinel nanoparticles, J. Inorg. Organomet. Polym. Mater. 34 (8) (2024) 3501–3510.
[18] A.R. Chakraborty, F.T.Z. Toma, K. Alam, S.B. Yousuf, K.S. Hossain, Influence of annealing temperature on Fe_2O_3 nanoparticles: synthesis optimization and structural, optical, morphological, and magnetic properties characterization for advanced technological applications, Heliyon 10 (21) (2024).
[19] M. Kosmulski, The pH-dependent surface charging and the points of zero charge, J. Colloid Interface Sci. 253 (1) (2002) 77–87.
[20] M. Kosmulski, pH-dependent surface charging and points of zero charge II, Update. *Journal of colloid and interface science* 275 (1) (2004) 214–224.
[21] M. Kosmulski, pH-dependent surface charging and points of zero charge: III, Update. *Journal of colloid and interface science* 298 (2) (2006) 730–741.
[22] M. Kosmulski, Surface Charging and Points of Zero Charge, CRC press, 2009.
[23] M. Kosmulski, The pH dependent surface charging and points of zero charge. X. Update, Adv. Colloid Interface Sci. 319 (2023) 102973.
[24] H. Guo, A.C. Marschilok, K.J. Takeuchi, E.S. Takeuchi, P. Liu, Rationalization of diversity in spinel MgFe2O4 surfaces, Adv. Mater. Interfaces 6 (22) (2019) 1901218.
[25] M. Kosmulski, pH-dependent surface charging and points of zero charge. IV. Update and new approach, J. Colloid Interface Sci. 337 (2) (2009) 439–448.
[26] M. Kosmulski, The pH-dependent surface charging and points of zero charge: V, Update. *Journal of colloid and interface science* 353 (1) (2011) 1–15.
[27] M. Kosmulski, The pH dependent surface charging and points of zero charge. VI. Update, J. Colloid Interface Sci. 426 (2014) 209–212.
[28] M. Kosmulski, The pH dependent surface charging and points of zero charge. VII. Update, Adv. Colloid Interface Sci. 251 (2018) 115–138.
[29] M. Kosmulski, The pH dependent surface charging and points of zero charge. VIII. Update, Adv. Colloid Interface Sci. 275 (2020) 102064.
[30] M. Kosmulski, The pH dependent surface charging and points of zero charge. IX. Update, Adv. Colloid Interface Sci. 296 (2021) 102519.
[31] I. Petrila, F. Tudorache, Annealing temperature effects on humidity sensor properties for Mg0. 5W0. 5Fe2O4 spinel ferrite, Sensors 22 (23) (2022) 9182.
[32] M. Tahir, M. Imran, Z.H. Shah, M.B. Riaz, S. Riaz, S. Naseem, Phase formation and dielectric properties of MgFe2O4 nanoparticles synthesized by hydrothermal technique, Heliyon 10 (8) (2024).
[33] T. Dippong, E.A. Levei, O. Cadar, Formation, structure and magnetic properties of MFe2O4@ SiO2 (M= co, Mn, Zn, Ni, cu) nanocomposites, Materials 14 (5) (2021) 1139.
[34] A. Sangeetha, K.V. Kumar, G.N. Kumar, Effect of annealing temperature on the structural and magnetic properties of NiFe 2 O 4 nanoferrites, Advances in Materials Physics and Chemistry 7 (02) (2017) 19.
[35] I. Petrila, F. Tudorache, The influence of li+ and K+ added cations and annealing temperature on the magnetic and dielectric properties of Mg-Zn ferrite, Materials 14 (17) (2021) 4916.
[36] K.D. McDonald, B.M. Bartlett, Microwave synthesis of spinel MgFe2O4 nanoparticles and the effect of annealing on photocatalysis, Inorg. Chem. 60 (12) (2021) 8704–8709.
[37] L. Lutterotti, P. Scardi, Simultaneous structure and size–strain refinement by the Rietveld method, Applied Crystallography 23 (4) (1990) 246–252.
[38] G.K. Williamson, W.H. Hall, X-ray line broadening from filed aluminium and wolfram, Acta Metall. 1 (1) (1953) 22–31.
[39] L. Weil, F. Bertaut, L. Bochirol, Propriétés magnétiques et structure de la phase quadratique du ferrite de cuivre, Journal de Physique et le Radium 11 (5) (1950) 208–212.
[40] B.D. Cullity, C.D. Graham, Introduction to Magnetic Materials, John Wiley & Sons, 2011.
[41] S. Landi Jr., I.R. Segundo, E. Freitas, M. Vasilevskiy, J. Carneiro, C.J. Tavares, Use and misuse of the Kubelka-Munk function to obtain the band gap energy from diffuse reflectance measurements, Solid State Commun. 341 (2022) 114573.
[42] M. Raghasudha, D. Ravinder, P. Veerasomaiah, Influence of Cr3+ ion on the dielectric properties of nano crystalline Mg-ferrites synthesized by citrate-gel method, Mater. Sci. Appl. 4 (7) (2013) 432–438.
[43] O'neill, H. S. C., Annersten, H., & Virgo, D., The temperature dependence of the cation distribution in magnesioferrite (MgFe2O4) from powder XRD structural refinements and Mössbauer spectroscopy, Am. Mineral. 77 (7–8) (1992) 725–740.
[44] S. Ram, S. Singh, Estimation of cation distribution in Zn0.5Mg0.5PrxFe2-xO4 ferrites using 57 Fe Mössbauer spectroscopy. International, J. Phys. 11 (2) (2023) 88–96.
[45] D. Lenaz, H. Skogby, F. Princivalle, U. Hålenius, The MgCr 2O4–MgFe2O4 solid solution series: effects of octahedrally coordinated Fe 3+ on T–O bond lengths, Phys. Chem. Miner. 33 (2006) 465–474.
[46] M. Naagar, S. Chalia, F. Wan, L.V. Panina, P. Thakur, P.B. Sharma, A. Thakur, Investigations on temperature-dependent magnetic properties and magnetic thermal stability of magnesium ferrite (MgFe2O4) nanoparticles, Journal of Magnetism and Magnetic Materials 592 (2024) 171798.
[47] D. Karoblis, K. Mazeika, R. Raudonis, A. Zarkov, A. Kareiva, Sol-gel synthesis and characterization of yttrium-doped MgFe2O4 spinel, Materials 15 (21) (2022) 7547.
[48] D.O. Okoroh, J.O. Ozuomba, S.O. Aisida, P.U. Asogwa, Properties of zinc ferrite nanoparticles due to PVP mediation and annealing at 500°C, Advances in nanoparticles 8 (02) (2019) 36.
[49] A. Pradeep, P. Priyadharsini, G. Chandrasekaran, Sol–gel route of synthesis of nanoparticles of MgFe2O4 and XRD, FTIR and VSM study, Journal of Magnetism and Magnetic Materials 320 (21) (2008) 2774–2779.
[50] J. Smit, H.P.J. Wijn, Ferrites, Cleaver, 1959.
[51] R.G. Kulkarni, H.H. Joshi, Comparison of magnetic properties of MgFe2O4 prepared by wet-chemical and ceramic methods, J. Solid State Chem. 64 (2) (1986) 141–147.
[52] A.K. Gupta, M. Gupta, Synthesis and surface engineering of iron oxide nanoparticles for biomedical applications, biomaterials 26 (18) (2005) 3995–4021.
[53] B. Henderson, G.F. Imbusch, Optical Spectroscopy of Inorganic Solids vol. 44, Oxford University Press, 2006.
[54] P.W. Atkins, R.G. Ratcliffe, J. de Paula, M. Wormald, Physical Chemistry for the Life Sciences, Oxford University Press, 2023.
[55] A. Blößer, H. Kurz, J. Timm, F. Wittkamp, C. Simon, S. Hayama, R. Marschall, Tailoring the size, inversion parameter, and absorption of phase-pure magnetic MgFe2O4 nanoparticles for photocatalytic degradations, ACS Appl. Nano Mater. 3 (11) (2020) 11587–11599.
[56] B. Choudhury, S. Bayan, A. Choudhury, P. Chakraborty, Narrowing of band gap and effective charge carrier separation in oxygen deficient TiO2 nanotubes with improved visible light photocatalytic activity, J. Colloid Interface Sci. 465 (2016) 1–10.

[57] F. Urbach, The long-wavelength edge of photographic sensitivity and of the electronic absorption of solids, Phys. Rev. 92 (5) (1953) 1324.
[58] K.K. Patankar, S.S. Joshi, B.K. Chougule, Dielectric behaviour in magnetoelectric composites, Phys. Lett. A 346 (5–6) (2005) 337–341.
[59] A. Radoń, D. Łukowiec, M. Kremzer, J. Mikuła, P. Włodarczyk, Electrical conduction mechanism and dielectric properties of spherical shaped Fe3O4 nanoparticles synthesized by co-precipitation method, Materials 11 (5) (2018) 735.
[60] B.K. Bammannavar, L.R. Naik, Electrical properties and magnetoelectric effect in (x) Ni0. 5Zn0. 5Fe2O4+ (1− x) BPZT composites, Smart Materials and Structures 18 (8) (2009) 085013.
[61] S. Singh, A. Kaur, P. Kaur, L. Singh, High-temperature dielectric relaxation and electric conduction mechanisms in a LaCoO3-modified Na0. 5Bi0. 5TiO3 system, ACS Omega 8 (28) (2023) 25623–25638.
[62] K. Iwauchi, Dielectric properties of fine particles of Fe3O4 and some ferrites, Jpn. J. Appl. Phys. 10 (11) (1971) 1520.
[63] K.S. Rane, V.M.S. Verenkar, P.Y. Sawant, Dielectric behaviour of MgFe2O4 prepared from chemically beneficiated iron ore rejects, Bull. Mater. Sci. 24 (2001) 323–330.
[64] S.J. Rzoska, A. Drozd-Rzoska, W. Bulejak, J. Łoś, S. Starzonek, M. Szafran, F. Gao, Critical insight into pretransitional behavior and dielectric tunability of relaxor ceramics, Materials 16 (24) (2023) 7634.
[65] R.G. Kharabe, R.S. Devan, C.M. Kanamadi, B.K. Chougule, Dielectric properties of mixed li–Ni–cd ferrites, Smart Mater. Struct. 15 (2) (2006) N36.
[66] B.M. Greenhoe, M.K. Hassan, J.S. Wiggins, K.A. Mauritz, Universal power law behavior of the AC conductivity versus frequency of agglomerate morphologies in conductive carbon nanotube-reinforced epoxy networks, J Polym Sci B 54 (19) (2016) 1918–1923.